

Continuous symmetry breaking in a trapped-ion spin chain

<https://doi.org/10.1038/s41586-023-06656-7>

Received: 22 November 2022

Accepted: 20 September 2023

Published online: 15 November 2023

 Check for updates

Lei Feng^{1,6}, Or Katz^{1,6}, Casey Haack², Mohammad Maghrebi³, Alexey V. Gorshkov⁴, Zhexuan Gong², Marko Cetina¹ & Christopher Monroe^{1,5}

One-dimensional systems exhibiting a continuous symmetry can host quantum phases of matter with true long-range order only in the presence of sufficiently long-range interactions¹. In most physical systems, however, the interactions are short-ranged, hindering the emergence of such phases in one dimension. Here we use a one-dimensional trapped-ion quantum simulator to prepare states with long-range spin order that extends over the system size of up to 23 spins and is characteristic of the continuous symmetry-breaking phase of matter^{2,3}. Our preparation relies on simultaneous control over an array of tightly focused individual addressing laser beams, generating long-range spin–spin interactions. We also observe a disordered phase with frustrated correlations. We further study the phases at different ranges of interaction and the out-of-equilibrium response to symmetry-breaking perturbations. This work opens an avenue to study new quantum phases and out-of-equilibrium dynamics in low-dimensional systems.

The exploration of new phases of matter has long been a frontier of physics. Quantum phases are particularly interesting, featuring non-local and macroscopic properties that have no classical counterpart⁴. One-dimensional quantum systems have captured special attention because they can often be efficiently described using various computational or analytic approaches^{2,5–7}. The microscopic form and range of the interaction between constituent particles directly determine the macroscopic properties and phases that such systems can exhibit. Perhaps the best example is the Mermin–Wagner theorem¹, which forbids low-dimensional short-range interacting systems with a continuous symmetry from exhibiting long-range order at any finite temperature.

One-dimensional systems with long-range interactions, by contrast, can manifest phases with long-range order^{2,3,8–17}. A prime example is a chain of spin 1/2 particles featuring long-range ferromagnetic interactions that have a continuous rotational $U(1)$ symmetry. In the absence of magnetic fields, the chain can possess an exotic phase in which the spins exist in a superposition of collective states in the symmetry plane with no preferred orientation, and the spontaneous breaking of the continuous symmetry manifests in sizeable magnetic correlations across the entire chain^{2,3}. Such a continuous symmetry-breaking (CSB) phase of matter has never been observed in a one-dimensional system.

Chains of trapped atomic ions are a pristine one-dimensional spin system, featuring high isolation from the environment, high-fidelity measurement and preparation of individual spins, and fully connected spin–spin interactions whose strength and range can be controlled by optical fields^{18–23}. There have been proposals for observing CSB in trapped-ion systems^{2,3}, requiring simultaneous control over each optical field addressing individual ions in a long and closely spaced crystal, which to date has been beyond experimental reach.

Here we report on continuous symmetry breaking in a one-dimensional trapped-ion quantum simulator. Using simultaneous individual control of a linear array of 23 optical beams addressing individual ions, we prepare the system in a CSB phase, manifesting long-range spin–spin correlations. Individual control over the spins enables the precise engineering and measurement of the interactions between spins as well as the study of non-equilibrium dynamics under symmetry-breaking perturbations. These results represent a frontier in the control of quantum phases and open new avenues in studying low-dimensional quantum systems.

The trapped-ion crystal under study comprises 27 ¹⁷¹Yb⁺ ions confined in a linear Paul trap on a chip^{24–26}, as illustrated in Fig. 1a. A fluorescence image of the crystal is shown in Fig. 1b. Each ion stores an effective spin comprising two ‘clock’ levels in its electronic ground state ($|\uparrow_z\rangle \equiv |F=1, M=0\rangle$ and $|\downarrow_z\rangle \equiv |F=0, M=0\rangle$) (ref. 27). We use a uniformly spaced array of tightly focused laser beams, together with an orthogonal wide global beam to simultaneously drive Raman transitions between the spin states of individual ions. The Raman addressing is sensitive to the motion along the wavevector difference between the individual and global addressing Raman beams¹⁸. The electrostatic trapping potential is configured to align the middle 23 ions with the array of individual addressing beams. The two pairs of non-illuminated edge ions facilitate the alignment of the 23 middle ions. The spins are initialized and measured using optical pumping and state-dependent fluorescence techniques²⁷ and the collective motional modes of the ion chain that mediate their interaction are cooled using sideband cooling²⁸. Single-spin rotations enable the orientation of each spin along any axis on the Bloch sphere for initialization or measurement.

We deform the spin Hamiltonian as a function of time for different initial states to prepare different quantum phases of matter. Specifically,

¹Duke Quantum Center, Department of Physics and Electrical and Computer Engineering, Duke University, Durham, NC, USA. ²Department of Physics, Colorado School of Mines, Golden, CO, USA.

³Department of Physics and Astronomy, Michigan State University, East Lansing, MI, USA. ⁴Joint Quantum Institute and Joint Center for Quantum Information and Computer Science, University of Maryland and NIST, College Park, MD, USA. ⁵IonQ, Inc., College Park, MD, USA. ⁶These authors contributed equally: Lei Feng, Or Katz. [✉]e-mail: leifeng@fudan.edu.cn; or.katz@duke.edu; monroe171@gmail.com

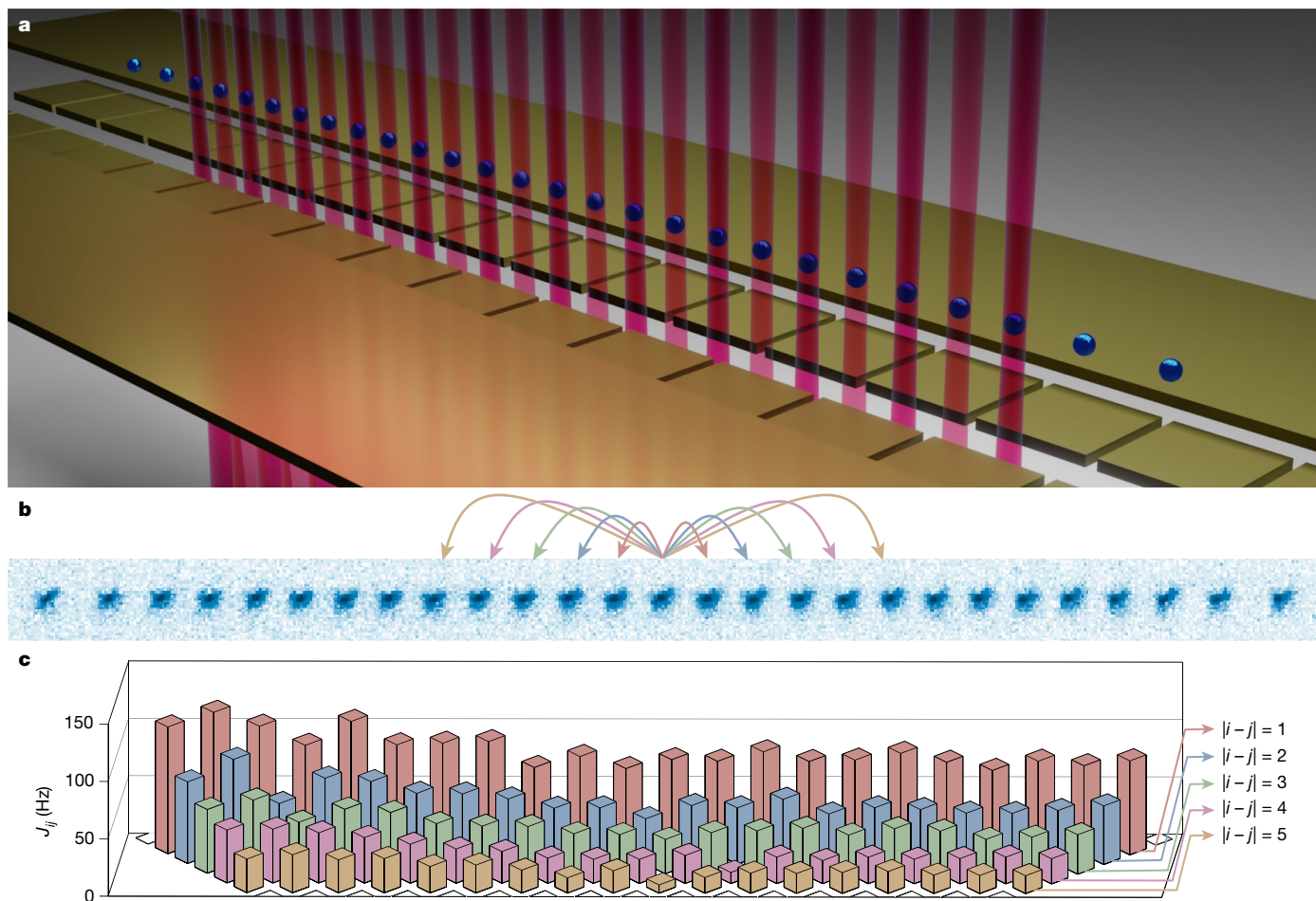


Fig. 1 | Trapped-ion crystal. **a**, Illustration of a one-dimensional crystal of 27 ions, confined in a linear Paul trap on a chip. A linear array of 23 tightly focused and individually controlled laser beams simultaneously generates site-dependent fields and a programmable interaction between the trapped-ion spins; an additional beam, propagating parallel to the trap surface, illuminates the entire ion chain from the side to facilitate these processes based on Raman

transitions (not shown). **b**, Fluorescence image of a crystal composed of 27 $^{171}\text{Yb}^+$ ions. **c**, Experimental reconstruction of the spin-spin interaction matrix J_{ij} of the 23 spins between the five nearest neighbours. The bars are horizontally aligned with the ion crystal image in **b**, and the colours indicate the interaction between spins at different distances $|i - j|$ (see Methods for the full modelled interaction).

we ramp down a staggered transverse-field Hamiltonian and ramp up an effective long-range XY Hamiltonian¹⁸ (Methods), so that the total time-dependent Hamiltonian is

$$H = \frac{s}{2} \sum_{i < j} J_{ij} (\hat{\sigma}_+^{(i)} \hat{\sigma}_-^{(j)} + \hat{\sigma}_-^{(i)} \hat{\sigma}_+^{(j)}) + (1-s) \sum_j h_j \hat{\sigma}_z^{(j)}, \quad (1)$$

where $s = s(t)$ is a time-dependent parameter changing from 0 to 1 during the time interval from $t = 0$ to $t = T$ and $\hat{\sigma}^{(j)}$ are the Pauli operators of the j -th ion. Here $h_j = (-1)^j h$ is a uniform-magnitude magnetic field with amplitude h that alternates between adjacent spins. Each interaction amplitude J_{ij} is positive and describes the flip-flop rate between the i -th and j -th spins.

The simultaneous time-dependent control of the Raman beams enables the generation of the staggered-field Hamiltonian. This control also allows the selection of a subset of N spins in the middle of the crystal that can interact with one another while remaining decoupled from the rest of the spins in the crystal: switching off the beam addressing the n -th ion nulls its hopping amplitude J_{in} to all other ions i . The individual control also enables the experimental reconstruction of the interaction matrix J_{ij} , as shown in Fig. 1c for the first five nearest neighbours ($|i - j| \leq 5$). Here, the measured long-range interaction decreases slowly as a function of the interspin spacing, where the spatial inhomogeneity is determined by the structure of the applied trapping potential.

The Hamiltonian evolution is also accompanied by decoherence induced by the optical drive (Methods).

To induce long-range correlations, we first initialize the spins in the Néel state in the z basis, corresponding to the highest excited state of the staggered-field Hamiltonian. We then ramp the Hamiltonian with the profile of $s(t)$ shown in Fig. 2a. After the ramp, we immediately measure the transverse correlations $C_{ij} = \langle \hat{\sigma}_+^{(i)} \hat{\sigma}_-^{(j)} + \hat{\sigma}_-^{(i)} \hat{\sigma}_+^{(j)} \rangle$. The measurements are performed simultaneously on all spins in the x and then in the y bases separately. To reduce statistical errors, each measurement is repeated 3,000 to 5,000 times, resulting in a 1σ binomial uncertainty 0.007 to 0.010 for each correlation C_{ij} . We first consider the time evolution for a subset of $N = 7$ interacting spins ($-3 \leq i, j \leq 3$) shown in Fig. 2b. As the staggered field decreases and the interaction increases, correlations develop between all the interacting spins in the x - y plane, indicating the CSB phase. On the other hand, when the spins are initialized in the ground state of the staggered-field Hamiltonian, shorter-range correlations develop in the x - y plane after evolving under the same ramp^{2,3}. Figure 2c presents the formation of alternating and fast-decaying correlations between the $N = 7$ interacting spins, indicating a disordered phase^{2,3}. We focus on the CSB phase and study the correlations at the end of the ramp for a different number of interacting spins in the same ion chain, shown in Fig. 3a and Extended Data Fig. 8. Dark blue spheres indicate the set of interacting ions that are illuminated by the addressing beams. In all configurations, we observe

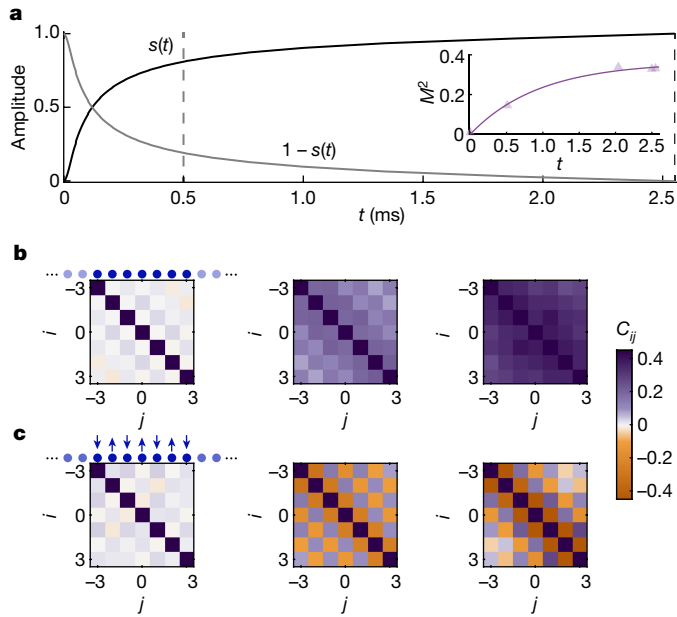


Fig. 2 | Preparation of quantum phases. **a**, Adiabatic ramp profiles of the effective XY Hamiltonian, $s(t)$, and the staggered magnetic field Hamiltonian, $1 - s(t)$, as a function of time t . The inset shows the average correlation $\mathcal{M}^2(N=7) = \frac{1}{21} \sum_{i < j} C_{ij}$, where experimental data points are represented by triangles and an exponential fit line is included to guide the eye. **b, c**, Measured spin-spin correlations $C_{ij} = \langle \hat{\sigma}_i^+ \hat{\sigma}_j^- + \hat{\sigma}_i^- \hat{\sigma}_j^+ \rangle$ developed during the ramp for the subset of $N=7$ interacting spins ($-3 \leq i, j \leq 3$) are indicated with small dark blue spheres; the other ions (light blue) are not addressed by optical fields and their spin states do not participate in the dynamics. **b**, Initializing the spins in the highest excited state of the staggered-field Hamiltonian along the z direction leads to a low-temperature state of the ferromagnetic XY Hamiltonian at the end of the ramp. The pronounced positive correlations between all interacting spins indicate the continuous symmetry-breaking (CSB) phase. **c**, Initializing the spins in the ground state of the staggered-field Hamiltonian prepares a low-temperature state of the antiferromagnetic XY Hamiltonian.

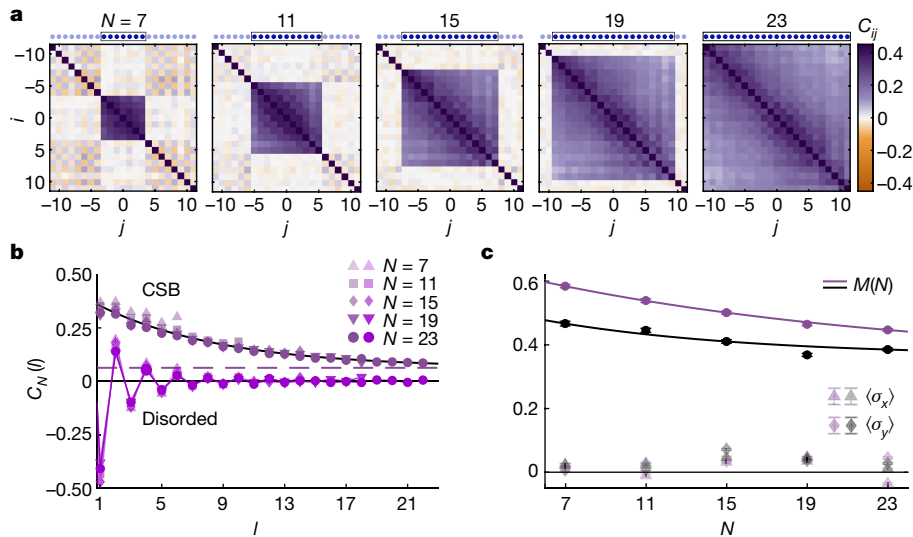


Fig. 3 | Long-range order. **a**, The measured correlation matrix C_{ij} of the prepared CSB phase for a subset of $N = 7, 11, 15, 19$ and 23 interacting spins. Dark blue spheres indicate the ions that are illuminated by the addressing beams. **b**, Spatially averaged correlations $C_N(l) = \frac{1}{N-l} \sum_j C_{j,j+l}$ as a function of the interspin distance l for different subsystem sizes N . The correlations in the CSB phase (greyish purple) saturate asymptotically at a non-zero value of 0.062 ± 0.005 in the $N, l \gg 1$ limit (dashed line), manifesting long-range order. By contrast, the staggered correlations of the disordered phase (magenta) decay quickly to zero. The shape and brightness of the symbols indicate the number of interacting spins N . **c**, The purple data for the order parameter of the CSB phase $\mathcal{M}(N)$ (equation (2))

sizeable and positive correlations C_{ij} between the interacting spins. To quantify the spatial dependence of the long-range order, we present the spatially averaged spin correlations $C_N(l) = \frac{1}{N-l} \sum_j C_{j,j+l}$ for different system sizes N as a function of the interspin distance $1 \leq l \leq N-1$ in Fig. 3b. The averaged correlations for different system sizes in the CSB phase nearly overlap and saturate to a non-zero value in the $N \gg 1$ and $l \gg 1$ limit indicated by the purple dashed line. The measured values of $C_N(l)$ also agree well with those from the numerical simulation of the experiment shown in Extended Data Fig. 6. The simulation takes into account single-qubit and collective decoherence processes present in our experiment, and is thus limited to $N \leq 11$ (see Methods for the technical details). By contrast, the spatially averaged correlations of the disordered phase alternate in sign and quickly decay to zero.

We further quantify the averaged correlation of the CSB phase by extracting the order parameter

$$\mathcal{M}(N) = \sqrt{\frac{1}{N(N-1)} \sum_{i \neq j} C_{ij}}, \quad (2)$$

as shown in Fig. 3c. The order parameter $\mathcal{M}(N)$ clearly saturates at a non-zero value, indicating the emergence of long-range order. We also note that the measured average correlation $\mathcal{M}^2(N)$ in our system is generally larger than the asymptotic correlation $C_N(\infty)$, due to the spatial variation of the correlations C_{ij} across the system.

On the other hand, the magnetizations in the x - y plane, obtained by averaging over N spins and over thousands of experimental repetitions, are nearly zero. This result is expected from the underlying $U(1)$ symmetry and the finite size of the chain. The average magnetization along z in the CSB phase and the average magnetizations in the disordered phase are presented in Extended Data Fig. 4. We point out that, for each cycle of the experiment, the measured spin magnetizations are in fact non-zero along the x or y direction (or any direction in the x - y plane), as indicated by the measured order parameter $\mathcal{M}(N)$ in Fig. 3c. The continuous $U(1)$ symmetry is therefore explicitly broken by symmetry-breaking measurements here. For a sufficiently large system

saturate asymptotically at a sizeable non-zero value of $B = 0.35 \pm 0.08$, while the average transverse magnetization in the x - y plane (pale symbols) is small, as expected from the continuous $U(1)$ symmetry in a finite system. Data in **a** and **b** as well as the purple data in **c** correspond to the interaction matrix that is partially shown in Fig. 1c. The black data in **c** corresponds to the interaction matrix that is partially shown in Extended Data Fig. 1 and exhibits a shorter interaction range. The black data for the order parameter saturates asymptotically at $B = 0.36 \pm 0.18$. Solid lines in **b** and **c** represent fits to $f(x) = Ae^{-x/L} + B$, where A, L and B are fitting parameters. Both configurations exhibit a similar B in light of the standard deviation errors that are estimated from the fit.

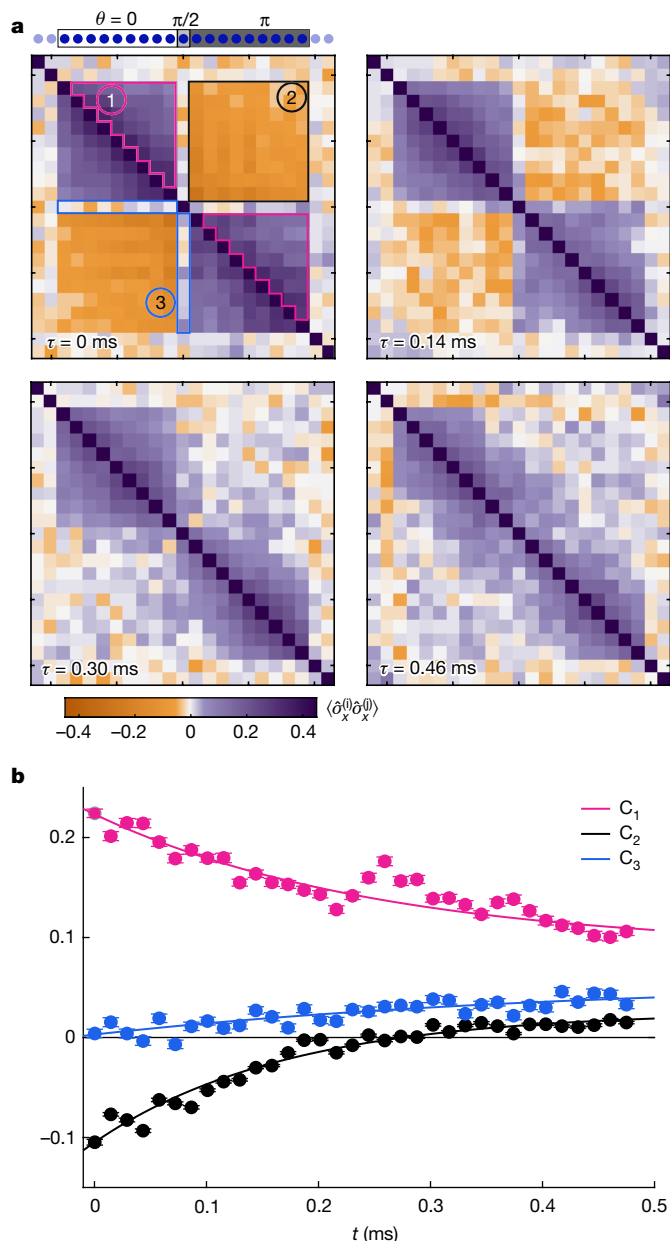


Fig. 4 | Out-of-equilibrium dynamics. Following the preparation of the CSB phase for $N = 19$ spins, we perturb the state by rotating the spins in the x - y plane by a spin-dependent angle θ at $\tau = 0$. **a**, Measured spin-spin correlations $\langle \hat{\sigma}_x^{(i)} \hat{\sigma}_x^{(j)} \rangle$ developed during the evolution by the effective XY Hamiltonian for time τ . At $\tau = 0$ (top left), spins within the right or within the left side of the chain feature positive correlations, while correlations between spins on different sides are negative. The middle spin has a near-zero correlation with the rest of the chain. At $\tau = 0.14$ ms (top right), the intercorrelations between the two sides decay quickly while the intracorrelations within each side are maintained. At later times (bottom) the entire chain develops positive correlations. **b**, Average correlation as a function of time. The dots in different colours correspond to the correlation averaged within the corresponding coloured contours shown in **a** (top left). Exponential fits with an offset (solid lines) are applied to guide the eye. The error bars indicate one standard error of the mean. The data in this figure correspond to the interaction matrix partially shown in Extended Data Fig. 1.

size, the continuous symmetry may also be broken spontaneously by generic symmetry-breaking perturbations.

The CSB phase is expected to persist in a system described by the XY Hamiltonian as long as the interactions have a sufficiently long range^{2,3}.

The dependence of the interaction range on optical Raman fields allows us to examine the relationship between the correlations and interaction range. We repeat the experiment with two other configurations exhibiting different interaction ranges, following a similar preparation protocol (Methods). In one configuration, which corresponds to the experimentally reconstructed interaction matrix J_{ij} shown in Extended Data Fig. 1 and Extended Data Fig. 5a (black curve), we prepare a spin state that exhibits long-range correlations, with a non-zero, yet smaller, order parameter for the CSB phase, as shown in Fig. 3c. In the other configuration, which has a considerably shorter interaction range as shown in Extended Data Fig. 5a (blue curve), we prepare a spin state that exhibits short-range correlations and is associated with a disordered phase (Extended Data Fig. 5b (right), c (blue)). These results highlight the key role played by the long-range interactions in realizing the emergent long-range order.

While the state we prepare is not in thermal equilibrium, we can estimate its effective temperature using numerical simulations. Here, we compare the correlations of our final state to those of a thermal state at the same energy. Our analysis, which focuses on the configuration corresponding to the black curve in Extended Data Fig. 5a, reveals that the final state has a low effective temperature T . For example, for $N = 11$, we find $k_B T \approx 0.07 \bar{E}_{\text{int}}$, where $\bar{E}_{\text{int}} = \frac{1}{N} \sum_{i \neq j} J_{ij}$ denotes the average value of the total interaction strength per spin and k_B is the Boltzmann constant. See Methods and Extended Data Fig. 9 for details.

We also utilized numerical simulations to model potential future experiments that could be conducted on our platform with larger system sizes and a wider range of interactions (Methods). These experiments would allow for the direct study of the exotic phase transition between the CSB phase and the disordered phase that is induced by changing the interaction range.

The simultaneous individual control over the Raman fields provides a probe to the CSB phase’s dynamical response to different perturbations. We observe the response of a perturbed CSB phase under the effective XY Hamiltonian in a system of $N = 19$ spins. We perturb the prepared CSB phase by rotating the spin of the individual ions by a variable angle θ_j about the z axis while maintaining them in the x - y plane. We invert the spins to the right of the centre ($j > 0$) ($\theta_j = \pi$) while leaving the spins to the left of the centre ($j < 0$) unperturbed ($\theta_j = 0$). The central spin ($j = 0$) is rotated by $\theta_0 = \pi/2$. This operation breaks the global $U(1)$ symmetry of the state while preserving the symmetry in the left and right subsystems.

Figure 4 shows the measured correlations $\langle \hat{\sigma}_x^{(i)} \hat{\sigma}_x^{(j)} \rangle$ as a function of the evolution time τ from state preparation at $\tau = 0$. Initially, the spins within each side ($i, j < 0$ or $i, j > 0$) of the crystal have positive correlations, while the correlations between spins on different sides are negative, as shown in Fig. 4a. During the evolution, the intercorrelations between the two sides decay faster than the intracorrelations within each side. At longer evolution times, the two sides of the crystal, as well as the middle spin, overcome the perturbation and develop positive correlations. In Fig. 4b, we show the full time evolution of the system by plotting the averaged correlation $C_n = \sum_{\{i,j\}} C_{ij}$ for $\{i, j\}$ taken within the coloured contours labelled as 1, 2, 3 in Fig. 4a, corresponding to $n = 1, 2, 3$, respectively. This demonstration shows our capability for further investigation of the properties of the symmetry-breaking phase. We have also performed numerical simulation of this quench experiment in the absence of dissipation. The simulation results, shown in Extended Data Fig. 7, agree qualitatively with the experimental data in Fig. 4.

In summary, we observe a continuous symmetry-breaking phase with long-range order in a one-dimensional spin chain, manifested at different interaction ranges. Moreover, we show the preparation of a disordered phase with fast-decaying staggered correlations. As a teaser on the study of non-equilibrium dynamics, we show the full time evolution of the perturbed CSB phase. This work opens new avenues for studying quantum phases of matter in low-dimensional systems.

The techniques presented in this work can be extended to study, for example, the phase diagram of the ferromagnetic XXZ model that was studied theoretically in ref. 3. This model extends the XY model studied in this work by adding an additional interaction term that couples spins in the z direction. Such a Hamiltonian can potentially be simulated using the techniques presented in refs. 17,29, which essentially involve adding a spatially uniform longitudinal field to the Hamiltonian we implement in equation (3). For example, applying a field that dominates the Ising interaction yields approximately the XXZ Hamiltonian, where the anisotropy of the interaction can be controlled through the orientation of the field with respect to the Ising interaction axis¹⁷. The additional longitudinal field term can be realized in a trapped-ion quantum simulator in a native manner¹⁸.

While completing this project, we became aware of a complementary demonstration of CSB in a two-dimensional Rydberg array³⁰.

Online content

Any methods, additional references, Nature Portfolio reporting summaries, source data, extended data, supplementary information, acknowledgements, peer review information; details of author contributions and competing interests; and statements of data and code availability are available at <https://doi.org/10.1038/s41586-023-06656-7>.

- Mermin, N. D. & Wagner, H. Absence of ferromagnetism or antiferromagnetism in one- or two-dimensional isotropic Heisenberg models. *Phys. Rev. Lett.* **17**, 1133 (1966).
- Gong, Z.-X. et al. Kaleidoscope of quantum phases in a long-range interacting spin-1 chain. *Phys. Rev. B* **93**, 205115 (2016).
- Maghrebi, M. F., Gong, Z.-X. & Gorshkov, A. V. Continuous symmetry breaking in 1d long-range interacting quantum systems. *Phys. Rev. Lett.* **119**, 023001 (2017).
- Sachdev, S. Quantum phase transitions. *Phys. World* **12**, 33 (1999).
- Giamarchi, T. *Quantum Physics in One Dimension*, Vol. 121 (Clarendon Press, 2003).
- Cazalilla, M., Citro, R., Giamarchi, T., Orignac, E. & Rigol, M. One dimensional bosons: from condensed matter systems to ultracold gases. *Rev. of Mod. Phys.* **83**, 1405 (2011).
- Chen, X., Gu, Z.-C. & Wen, X.-G. Classification of gapped symmetric phases in one-dimensional spin systems. *Phys. Rev. B* **83**, 035107 (2011).
- Haldane, F. D. M. Nonlinear field theory of large-spin heisenberg antiferromagnets: semiclassically quantized solitons of the one-dimensional easy-axis Néel state. *Phys. Rev. Lett.* **50**, 1153 (1983).
- Dalla Torre, E. G., Berg, E. & Altman, E. Hidden order in 1d bose insulators. *Phys. Rev. Lett.* **97**, 260401 (2006).
- Gong, Z.-X. et al. Topological phases with long-range interactions. *Phys. Rev. B* **93**, 041102 (2016).

- Ren, J., Wang, Z., Chen, W. & You, W.-L. Long-range order and quantum criticality in antiferromagnetic chains with long-range staggered interactions. *Phys. Rev. E* **105**, 034128 (2022).
- Li, Z., Choudhury, S. & Liu, W. V. Long-range-ordered phase in a quantum heisenberg chain with interactions beyond nearest neighbors. *Phys. Rev. A* **104**, 013303 (2021).
- Herbrych, J. et al. Block-spiral magnetism: An exotic type of frustrated order. *Proc. Natl Acad. Sci. USA* **117**, 16226 (2020).
- Giachetti, G., Trombettoni, A., Ruffo, S. & Defenu, N. Berezinskii-Kosterlitz-Thouless transitions in classical and quantum long-range systems. *Phys. Rev. B* **106**, 014106 (2022).
- Potirniche, I.-D., Potter, A. C., Schleier-Smith, M., Vishwanath, A. & Yao, N. Y. Floquet symmetry-protected topological phases in cold-atom systems. *Phys. Rev. Lett.* **119**, 123601 (2017).
- Patrick, K., Neupert, T. & Pachos, J. K. Topological quantum liquids with long-range couplings. *Phys. Rev. Lett.* **118**, 267002 (2017).
- Bermúdez, A., Tagliacozzo, L., Sierra, G. & Richerme, P. Long-range Heisenberg models in quasiperiodically driven crystals of trapped ions. *Phys. Rev. B* **95**, 024431 (2017).
- Monroe, C. et al. Programmable quantum simulations of spin systems with trapped ions. *Rev. Mod. Phys.* **93**, 025001 (2021).
- Blatt, R. & Roos, C. F. Quantum simulations with trapped ions. *Nat. Phys.* **8**, 277 (2012).
- Joshi, M. K. et al. Observing emergent hydrodynamics in a long-range quantum magnet. *Science* **376**, 720 (2022).
- Zhang, J. et al. Observation of a many-body dynamical phase transition with a 53-qubit quantum simulator. *Nature* **551**, 601 (2017).
- Morong, W. et al. Observation of stark many-body localization without disorder. *Nature* **599**, 393 (2021).
- Dumitrescu, P. T. et al. Dynamical topological phase realized in a trapped-ion quantum simulator. *Nature* **607**, 463 (2022).
- Maunz, P. L. W. *High Optical Access Trap 2.0*. Technical Report (Sandia National Lab., 2016).
- Egan, L. et al. Fault-tolerant control of an error-corrected qubit. *Nature* **598**, 281–286 (2021).
- Katz, O., Feng, L., Risinger, A., Monroe, C. & Cetina, M. Demonstration of three- and four-body interactions between trapped-ion spins. *Nat. Phys.* <https://doi.org/10.1038/s41567-023-02102-7> (2023).
- Olmschenk, S. et al. Manipulation and detection of a trapped Yb^+ hyperfine qubit. *Phys. Rev. A* **76**, 052314 (2007).
- Egan, L. N. *Scaling Quantum Computers with Long Chains of Trapped Ions*. Ph.D. thesis, Univ. of Maryland (2021).
- Ciavarella, A. N., Caspar, S., Illa, M. & Savage, M. J. State preparation in the Heisenberg model through adiabatic spiraling. *Quantum* **7**, 970 (2023).
- Chen, C. et al. Continuous symmetry breaking in a two-dimensional Rydberg array. *Nature* **616**, 691 (2023).

Publisher's note Springer Nature remains neutral with regard to jurisdictional claims in published maps and institutional affiliations.

Springer Nature or its licensor (e.g. a society or other partner) holds exclusive rights to this article under a publishing agreement with the author(s) or other rightsholder(s); author self-archiving of the accepted manuscript version of this article is solely governed by the terms of such publishing agreement and applicable law.

© The Author(s), under exclusive licence to Springer Nature Limited 2023

Interaction Hamiltonian

We generate spin–spin interactions using Raman transitions that virtually excite collective motion of the ions. The beam that globally addresses the ion chain traverses an acousto-optical modulator that is simultaneously driven with two radio-frequency signals, splitting the optical beam into two components with distinct tones. These two tones drive simultaneously the first red and blue sideband transitions in the dispersive regime with symmetric detunings Δ of the Raman beatnote from the highest-frequency mode of the ion chain. We control the radial electrostatic potential to spectrally separate the two sets of radial modes and to align the wavevector difference of the Raman fields to the addressed set. In this configuration, we realize the Ising Hamiltonian $H_{\text{XX}}(t) = s(t) \sum_{ij} J_{ij} \hat{\sigma}_x^{(i)} \hat{\sigma}_x^{(j)}$. The time dependence of the Ising Hamiltonian is realized by varying the Rabi frequencies of the ions by a factor of $\sqrt{s(t)}$; this is achieved by controlling the power of N (greater than 23) radio-frequency signals feeding a multichannel acousto-optical modulator which modulates the amplitude of the individually addressing beams, while turning off all other $(23 - N)$ channels.

We apply an effective transverse field at each spin by shifting the frequency of the beam addressing the j -th ion as a function of time by $f_j = 2s(t)B + 2(1 - s(t))(-1)^j/h$, where B is a spatially uniform transverse field. This combination generates the transverse-field Hamiltonian that is composed of two terms: a spatially uniform transverse field Hamiltonian $H_B = s \sum_j B \hat{\sigma}_z^{(j)}$ and a staggered field Hamiltonian $H_h = (1 - s) \sum_j h(-1)^j \hat{\sigma}_z^{(j)}$. The total experimentally applied time-dependent Hamiltonian is therefore

$$H' = H_{\text{XX}} + H_B + H_h. \quad (3)$$

The longer-range configuration with the interaction matrix in Fig. 1c and purple curve in Extended Data Fig. 5a corresponds to $\Delta \approx 2\pi \times 20$ kHz, $B = 2\pi \times 1.6$ kHz, $h = 2\pi \times 0.9$ kHz, and a ramp time of $T = 2.55$ ms. The average nearest-neighbour interaction strength is $\bar{J} = \frac{1}{N-1} \sum_i J_{i,i+1} = 2\pi \times 0.09$ kHz. The second configuration with the interaction matrix in Extended Data Fig. 1 and black curve in Extended Data Fig. 5a corresponds to $\Delta \approx 2\pi \times 55$ kHz, $B = 2\pi \times 6.5$ kHz, $h = 2\pi \times 4.2$ kHz, a ramp time of $T = 0.54$ ms, and $\bar{J} = 2\pi \times 0.5$ kHz. The third configuration with the interaction profile shown in Extended Data Fig. 5a (blue) corresponds to $\Delta \approx (\omega_1 - \omega_{27}) - 2\pi \times 500$ kHz (detuned by about $2\pi \times 200$ kHz from the zig-zag mode), $B = 2\pi \times 430$ Hz, $h = 2\pi \times 330$ Hz, a ramp time of $T = 4.4$ ms, and $\bar{J} = 2\pi \times 50$ Hz. We set the values of the Rabi amplitudes Ω_i to ensure that the nearest-neighbour interactions satisfy $J_{i,i+1} = \bar{J}$ (equation (4)). However, this leads to inhomogeneous light shifts due to the non-uniformity of the Rabi amplitudes. To address this, we independently calibrate and compensate for the inhomogeneity during the experiment by adding an effective site-dependent magnetic field. Moreover, we make sure that the evolution is represented by $J_{ij} > 0$ for this configuration. We correct for the staggered sign of the J_{ij} matrix that is obtained from equation (4) through the application of a staggered spin-phase, which corresponds to the transformation $\hat{\sigma}_x^{(i)} \rightarrow -\hat{\sigma}_x^{(i)}$ for odd i in $H_{\text{XX}}(t)$.

The applied transverse field overwhelms the Ising interaction because $B \gg \bar{J}$. Using the definition of the raising and lowering spin operators, $\hat{\sigma}_\pm^{(i)} = \frac{1}{2}(\hat{\sigma}_x^{(i)} \pm i\hat{\sigma}_y^{(i)})$, we can represent the Ising interaction in a frame rotating at the Larmor frequency of the uniform field by $\hat{\sigma}_x^{(i)} \hat{\sigma}_x^{(j)} \approx \frac{1}{2}(\hat{\sigma}_+^{(i)} \hat{\sigma}_-^{(j)} + \hat{\sigma}_-^{(i)} \hat{\sigma}_+^{(j)})$, bestowing fast oscillations to the $\hat{\sigma}_\pm^{(i)} \hat{\sigma}_\pm^{(j)}$ terms. This construction produces the effective XY Hamiltonian described in the main text.

The inhomogeneity in the experimentally measured J_{ij} primarily originates from the structure of the mode participation factors b_{nk} , which determine the extent to which the n -th ion participates in the k -th phonon mode. To achieve long-range interactions, we detuned our Raman

lasers far from the mode spectrum but on the side of the centre-of-mass mode, which is the highest-frequency mode whose participation factors are most uniform. In an ideal scenario, the non-uniformity of the mode participation factors would lead to a variation of about 3% in the nearest-neighbour spin–spin coupling across the chain, assuming uniform Raman power for all ions. However, the larger experimental non-uniformity is attributed to additional variation in the mode participation factors. After the experiment was conducted, we discovered that this variation was likely caused by a defective connection of one of the electrodes that make up the ion trap, which led to an inhomogeneity of the electrostatic trapping potential.

Experimental reconstruction of the J_{ij} matrix

We measure each J_{ij} element by turning on the two beams addressing the i -th and j -th ions while turning off all other beams in the array. The ions are initialized in the state $|\uparrow_z^{(i)} \downarrow_z^{(j)}\rangle$ for $j > i$, and the transverse field is adjusted to zero ($f_i = f_j = 0$). We apply a constant-amplitude pulse with a Rabi frequency that is scaled by a factor $g = 1.3$ in the first configuration (interaction matrix in Fig. 1) and by $g = 1$ in the second configuration (interaction matrix in Extended Data Fig. 1) and measure the population oscillations. We fit the average staggered magnetization $\frac{1}{2}(\hat{\sigma}_z^{(i)} - \hat{\sigma}_z^{(j)})$ to the function $\exp(-\Gamma_{ij}t) \cos(\pi g^2 J_{ij} t)$ using J_{ij} and Γ_{ij} as fitting parameters. The measured values of Γ_{ij} are given in Extended Data Fig. 2, and an example of the reconstruction is shown in Extended Data Fig. 3.

Numerical calculation of the J_{ij} matrix

We calculate the interaction matrix J_{ij} that results from applying a spin-dependent optical dipole force with the Raman lasers, following refs. 18,31. These lasers generate coupling between the spins and the collective motional modes along a single radial direction, virtually exciting phonons that mediate the spin–spin interaction.

$$J_{ij} = \sum_k \frac{\eta_{ik} \eta_{jk} \Omega_i \Omega_j}{2(\Delta + \omega_1 - \omega_k)}. \quad (4)$$

The spin–motion coupling matrix is represented by the Lamb–Dicke parameters $\eta_{nk} = 0.08 b_{nk}$, where b_{nk} is the mode participation matrix element describing the coupling between spin n and motional mode k (ref. 26). We numerically calculate the matrix b_{nk} and the frequencies of the motional modes ω_k , listed in decreasing order, for the applied trapping potentials; we consider a quadratic trapping potential in the radial direction with centre-of-mass frequency $\omega_1 = 2\pi \times 3.3$ MHz and an axial potential of $V(x) = 250 \times x^4 - 0.1 \times x^2$, where x is the coordinate along the chain axis in millimetres and V is the axial electrostatic potential in electron volts. This potential yields a nearly uniform-spaced ion chain for the inner 23 ions with a spacing of 3.75 μm . Ω_i represents the equivalent resonant carrier Rabi frequency at ion i , and we assume a spatially uniform profile.

In Extended Data Fig. 5 we present the numerically calculated averaged interaction $J(l) = \frac{1}{N-l} \sum_i J_{i,i+l}$ as a function of the distance l for the three configurations (circles), where $\bar{J} \equiv J(1)$. To calculate the spin–spin interaction, we model our radial trapping potential as harmonic and the axial trapping potential with a fourth-degree polynomial. We adjust the coefficients of each term in the polynomial expansion to match the interion spacing in the experiment, using a procedure similar to that described in ref. 28,32. Next, we compute the mode frequencies and mode participation factors. Finally, we use equation (4) to determine the spin–spin coupling, given the Raman beatnote detuning and Rabi frequencies. We also present the average experimentally measured interaction (open squares), where the bars reflect the total spread of values between different pairs, excluding points for which the error in the reconstructed value exceeded the actual measured value (only for several elements with $l = 5$ in the second configuration which appear in Extended Data Fig. 1 as zero). The measured and the

calculated values are in a good agreement. We fit the theoretical values to the fitting function

$$J(l) = \bar{J} e^{-\beta'(l-1)} l^{-\alpha'}, \quad (5)$$

which we adapt from ref. 33. The fitted parameters are $\alpha' = 0.44$, $\beta' = 0.19$ for the first configuration (purple line), $\alpha' = 1$, $\beta' = 0.19$ for the second configuration (black line) and $\alpha' = 3.4$, $\beta' = 0.0$ for the third configuration (blue line).

Numerical simulation of the experiments

Here we describe the details of the numerical simulation we performed in this paper. We numerically simulate the evolution of the experimentally prepared initial state (Fig. 2b) under the time-dependent Hamiltonian H' in equation (3). The Ising interaction matrix $\{J_{ij}\}$ is obtained using equation (4), normalized such that the average nearest-neighbour interaction matches the experimentally measured values (Fig. 1c). Particularly, we take into account two major sources of decoherence that likely exist in our experiment: Each qubit i is subject to an individual dephasing rate γ_i along the x direction and additionally, all qubits decohere collectively at rate γ_c primarily due to the heating of the centre-of-mass phonon mode. The density matrix of the system ρ then evolves according to the following master equation:

$$\begin{aligned} \frac{d\rho}{dt} = & -\frac{i}{\hbar} [H'(t), \rho] - \left[\sum_i \gamma_i (\rho - \hat{\sigma}_x^{(i)} \rho \hat{\sigma}_x^{(i)}) \right. \\ & \left. - \gamma_c \left[\frac{\hat{S}_z^2 \rho + \rho \hat{S}_z^2}{2} - \hat{S}_z \rho \hat{S}_z \right] \right], \quad (6) \end{aligned}$$

where $\hat{S}_z = \sum_i \hat{\sigma}_z^{(i)}$ represents the collective Pauli operator. The values of γ_i and γ_c are obtained by performing the best fit to the measured pairwise decoherence rate matrix $\{r_{ij}\}$ shown in Extended Data Fig. 2. We then calculate $\{C_N(l)\}$ and compare them with their experimental values from Fig. 3b. Such comparison is shown in Extended Data Fig. 6 for either $N = 7$ or $N = 11$. A good agreement between the theory and experiment is observed, except for some boundary effects that are more pronounced in the theory. Simulation for $N \geq 15$ qubits with decoherence is beyond our current numerical simulation capability.

In addition, we also simulated the unitary quench dynamics experiment (in the absence of decoherence). In this case, we are evolving the state only under the Hamiltonian in equation (3), which allows us to simulate the experiment for $N = 19$ qubits. The results are shown in Extended Data Fig. 7, which agree qualitatively with the experimental counterparts in Fig. 4. The fast oscillations in the numerical simulation are due to the large transverse field (H_B in equation (3)) we applied to simulate the XY interaction. The lack of oscillations and the smaller values of correlations observed experimentally are likely due to the effects of decoherence.

To show that the experimentally prepared state at the end of the ramp is approximately described as a low-temperature thermal state, we first calculate the energy E of the experimental state with respect to the ferromagnetic XY Hamiltonian (the negative of H defined in equation (1) with $s = 1$). This calculation is made possible by our experimental measurements of $\langle \hat{\sigma}_x^{(i)} \hat{\sigma}_x^{(j)} \rangle$ and $\langle \hat{\sigma}_y^{(i)} \hat{\sigma}_y^{(j)} \rangle$ for all pairs of (i, j) , as shown in Extended Data Fig. 8. We then numerically find an effective temperature \mathcal{T} such that the thermal state $\rho_{\mathcal{T}} = e^{H/(k_B \mathcal{T})} / \text{Tr} [e^{H/(k_B \mathcal{T})}]$ also has energy E . We then compare the experimentally measured correlations $C_N(l)$ (Fig. 3c) with those calculated in the thermal state. An example of such a comparison for the second experimental configuration (black curve in Extended Data Fig. 5a) and $N = 11$ is shown in Extended Data Fig. 9. We find a reasonable agreement between the correlations in the two states, with $k_B \mathcal{T} = 2\pi \times 0.03$ kHz, taking $\hbar = 1$ in the simulation. As the average interaction strength per spin is about

$2\pi \times 0.43$ kHz, we see that the experimental state can be regarded as a low-temperature state.

Our platform has the potential to enable future experiments with larger system sizes, which could allow us to study the phase transition between the CSB phase and the disordered phase by changing the interaction range. To illustrate this possibility, we have numerically simulated the order parameter $\mathcal{M}(N)$ (defined in equation (2)) in the ground state of $-H$ (where H is defined in equation (1), with $s = 1$) for system sizes $N = 23$, $N = 49$ and $N = 89$, using a variational matrix product state algorithm³⁴. For each value of N , we compute the interaction matrix J_{ij} by fixing the values of the axial trapping potential (taken as a sixth order polynomial) to generate an ion chain with approximately uniform ion distances. We then scan the interaction profiles that can be achieved using the single parameter Δ , which corresponds to the sideband detuning relative to the centre-of-mass mode. Finally, we use an approximate form by fitting the interaction matrix to equation (5) for each detuning.

We plot $\mathcal{M}(N)$ as a function of the sideband detuning Δ in Extended Data Fig. 10. Increasing Δ from 0 to ∞ monotonically decreases the interaction range from all-to-all to dipolar. As the system size increases, the order parameter $\mathcal{M}(N)$ of the CSB phase undergoes a sharper change as the interaction range is decreased, indicating a phase transition out of the CSB phase. This phase transition is of infinite order, making it difficult to find the exact phase transition point even for systems with a few hundred spins³. However, approximate calculations using either spin-wave theory or field theory can be used to predict the phase transition point in the limit of large system sizes³.

Effect of boundaries and disorder

Here, we analyse the effect of boundaries as well as the variation in the interaction profile in both the disordered/XY phase (characterized by power-law decaying correlations) and the CSB phase (with long-range order). Specifically, we argue that (1) boundaries lead to a faster decay of correlations in the XY phase (owing to the significant role played by fluctuations) while the CSB phase is rather insensitive to the boundaries and (2) the CSB phase is robust against some amount of variation in J_{ij} .

Point (1) implies that boundaries tend to weaken long-range correlations in the XY phase but are inconsequential in the CSB phase. This observation rules out the possibility that long-range order could be an artefact of boundary effects.

Point (2) shows that the CSB phase is robust against the non-uniformity of the interaction profile. This is particularly important since the interaction profile J_{ij} in the experimental setting is rather non-uniform for a given separation $|i - j|$. While the non-uniformity of the experimentally measured J_{ij} originates from the experimental settings we realize (particularly the shape of the trapping potential), in the analysis below, we also consider disorder in J_{ij} caused by fluctuations of parameters from one experiment to another and study the behaviour of the XY and CSB phases at weak disorder strength. We note that there is also some degree of uncertainty on the measured J_{ij} that is especially pronounced at larger separations $|i - j|$, owing to their weaker values compared to nearest-neighbour J_{ij} and the presence of decoherence.

Effect of boundaries

Short-range interactions. The XY model with short-range interactions can be described by an effective Hamiltonian in the continuum limit as⁵

$$H_{\text{SR}} = \frac{u}{2\pi} \int dx \frac{1}{K} (\partial_x \phi)^2 + K (\partial_x \theta)^2, \quad (7)$$

where the bosonic variables ϕ and θ provide a bosonization of the spin variables. Roughly speaking, the field θ gives the spin orientation in the x - y plane, $S_j^x = S_j^x \pm S_j^y \approx e^{\pm i\theta(x_j)}$, while the gradient of ϕ characterizes the spin component along the z axis. These bosonic variables are conjugate, that is, they satisfy $[\partial_x \phi(x), \theta(x')] = i\pi \delta(x - x')$. The parameter

Article

K is the so-called Luttinger parameter; specifically, $K = 1$ for the nearest-neighbour XY model. An effective action can be derived in terms of one of the two variables as

$$I = \frac{K}{2\pi u} \int dx d\tau [(\partial_\tau \theta)^2 + (\partial_x \theta)^2], \quad (8)$$

which determines the nature of (phase) fluctuations. These fluctuations destroy any kind of ordering:

$$\langle S^\pm \rangle \approx e^{-\frac{1}{2} \langle \theta^2 \rangle} \rightarrow 0, \quad (9)$$

as $\langle \theta^2 \rangle = \int_{1/N}^1 dq/q \approx \log N$ diverges logarithmically with system size N , in agreement with the Mermin–Wagner theorem. These fluctuations, however, give rise to long-range correlations (but not ordering) defined by

$$\langle S_i^+ S_j^- \rangle \approx e^{-\frac{1}{2} \langle (\theta(x_i) - \theta(x_j))^2 \rangle}, \quad (10)$$

where x_i represents the position corresponding to the lattice point i . For an infinite system (or a finite system well within the bulk, away from the boundaries), we have

$$\begin{aligned} \langle (\theta(x) - \theta(y))^2 \rangle &= \frac{1}{K} \int dq \frac{1 - \cos q(x-y)}{q} \\ &\approx \frac{1}{K} \log|x-y|, \end{aligned} \quad (11)$$

where $|x-y| \gg 1$. It then follows from equation (10) that the spin correlations decay as $1/|x-y|^{1/(2K)}$.

Next, we consider an open spin chain with a boundary at $x = 0$. In the continuum limit, this corresponds to a ‘fixed-end’ boundary condition for the field ϕ (ref. 5). The latter variable is conjugate to θ with the commutation relation $[\partial_x \phi(x), \theta(x')] = i\pi \delta(x-x')$. Fixing the field ϕ then dictates a free boundary condition for θ , that is, $\partial_x \theta(0) = 0$. The phase fluctuations are then given by

$$\begin{aligned} \langle (\theta(x) - \theta(y))^2 \rangle &= \frac{1}{K} \int dq \frac{(\cos(qx) - \cos(qy))^2}{q} \\ &\approx \frac{3}{2K} \log|x-y|, \end{aligned} \quad (12)$$

roughly when $x \approx 1$ is close to the boundary while y is far away. Notice that the coefficient of the logarithm is larger than that in equation (11) and thus leads to a faster decay of correlations approximately equal to $1/|x-y|^{3/(4K)}$. Therefore, bulk-boundary correlations decay faster than correlations well within the bulk. This should be expected because the field θ , corresponding to a free end, is highly fluctuating at the edge. In short, the existence of a boundary suppresses long-range correlations. For sufficiently large systems, these predictions can be verified using matrix product state algorithms. For smaller system sizes, the same qualitative trend persists although correlations do not exactly fall off as a power law.

Long-range interactions

The long-range interactions in our experiment take the form of $J_l e^{-l/R}$ $l^{-\alpha}$, where l is the distance between two spins. If R is proportional to the system size, this interaction pattern is not very different from the simple $1/l^\alpha$ power-law-decay interaction pattern. Therefore, for simplicity, in this analysis, we assume a long-range interacting XY Hamiltonian of the form $\sum_{|i-j|^\alpha} (S_i^+ S_j^- + S_i^- S_j^+)$. This Hamiltonian leads to a long-range term in the continuum limit³:

$$H_{LR} \approx - \int_{LR} dx dy \frac{1}{|x-y|^\alpha} \cos[\theta(x) - \theta(y)]. \quad (13)$$

The integral is computed over all x and y for $|x-y| > \lambda$ with λ a short-wavelength cutoff (for example, lattice spacing). If the long-range interactions are relevant, the system becomes ordered, say along the x direction, and the Hamiltonian can be expanded around $\theta = 0$. The effective field theory describing this phase is given by³

$$I = \int d\tau dx (\partial_\tau \theta)^2 + \int_{LR} \frac{d\tau dx dy}{|x-y|^\alpha} (\theta(x, \tau) - \theta(y, \tau))^2. \quad (14)$$

We can then determine the dynamic exponent z and the scaling dimension $[\theta]$ as³

$$z = \frac{\alpha-1}{2}, \quad [\theta] = \frac{3-\alpha}{4}. \quad (15)$$

The scaling dimension (θ) determines the decay of the phase correlations in the CSB phase: $\langle \theta(x)\theta(y) \rangle \approx 1/|x-y|^{2[\theta]}$. The latter correlations are due to fluctuations on top of long-range order, which implies $\langle S_i^+ S_j^- \rangle \rightarrow$ constant at large separations.

In contrast with the XY phase, fluctuations in the CSB phase only lead to a slight suppression of the order parameter: $\langle S^\pm \rangle \approx \exp(-\langle \theta^2 \rangle/2)$, where $\langle \theta^2 \rangle \approx \int dq/q^z$ with z the dynamic exponent in the CSB phase in equation (15). The dynamical exponent $z < 1$ describes a nonlinear light cone owing to the long-range interactions³. The fact that $z < 1$ renders the above integral finite, and the order parameter remains finite. Furthermore, this means that the CSB phase could only occur for $z < 1$, which implies $\alpha \leq 3$ (ref. 3). On similar grounds, one can see that the boundary has little effect on the order parameter or on the correlations because it only modifies the fluctuations, which are inconsequential in the CSB phase.

Effect of disorder in J_{ij}

We now consider the effect of disorder in the interaction profile $\{J_{ij}\}$ in our experiment. To be specific, we assume that either the mode structure coefficients $\{\eta_{i,k}\}$ or the Rabi frequencies $\{\Omega_i\}$ (or both) in equation (4) have small (relative to their expected values) fluctuations from one experiment to another. Such fluctuations effectively lead to fluctuations in J_{ij} that take the approximate form $J_{ij}(1 + \delta_i + \delta_j)$, where $\{\delta_i\}$ are assumed to be small, independent random variables with zero mean and standard deviation D . As the spin correlations we measure come from an average over many experiments with each having a slightly different interaction profile $\{J_{ij}\}$, the fluctuations in J_{ij} effectively lead to disorder.

Again assuming for simplicity that $J_{ij} \approx 1/|i-j|^\alpha$, the effective Hamiltonian corresponding to the disordered interaction in the continuum limit then becomes

$$H_{Dis} = \sum_{i < j} \frac{\delta_i + \delta_j}{|i-j|^\alpha} \cos(\theta(x_i) - \theta(x_j)). \quad (16)$$

In the CSB phase, we expand around $\theta = 0$ to find a quadratic term in $\theta(x_i) - \theta(x_j)$. Performing the average over disorder using the replica trick⁵, we obtain the effective action

$$\begin{aligned} I_{Dis} &\approx -D \sum_i \left[\int d\tau \sum_j \sum_{a=1}^n \frac{(\theta_a(x_i, \tau) - \theta_a(x_j, \tau))^2}{|i-j|^\alpha} \right] \\ &\rightarrow -D \sum_{a,b=1}^n \int_{LR} \frac{d\tau d\tau' dx dy dy'}{|x-y|^\alpha |x-y'|^\alpha} \\ &\quad \times (\theta_a(x, \tau) - \theta_a(y, \tau))^2 (\theta_b(x, \tau') - \theta_b(y', \tau'))^2, \end{aligned} \quad (17)$$

where $a = 1, 2, \dots, n$ denote the replicas; the second line in equation (17) is obtained in the continuum limit. A simple scaling analysis then shows that the strength of disorder D decreases under rescaling ($x \rightarrow e^{-l}x$) as

$$\frac{dD}{dl} = (3 + 2z - 2\alpha - 4[\theta])D = -D, \quad (18)$$

where we used equation (15). This result implies that the disorder is irrelevant in the CSB phase.

For $\alpha < 1$, the Hamiltonian is super-extensive (that is, the energy density increases with system size), and the above analysis should be modified. It is convenient to divide the Hamiltonian by a (Kac) normalization factor defined as $\mathcal{N} = \frac{1}{N-1} \sum_{ij} J_{ij} \approx N^{1-\alpha}$, rendering the Hamiltonian extensive³⁵. Such normalization only affects the overall energy scales and does not change the phase of the system. The ground state of the XY Hamiltonian with $\alpha < 1$ is always in the CSB phase^{2,3}. One can see this, for example, from the spin-wave analysis assuming a CSB phase where all the spins are polarized along the +x direction. A Holstein–Primakoff mapping gives $S_i^x = 1 - 2a_i^\dagger a_i$ and $S_i^y \approx a_i + a_i^\dagger$. The Hamiltonian then becomes²

$$H = \sum_k (a_k^\dagger \ a_{-k}) \begin{pmatrix} -\frac{\tilde{J}_k}{2\mathcal{N}} + 1 & -\frac{\tilde{J}_k}{2\mathcal{N}} \\ -\frac{\tilde{J}_k}{2\mathcal{N}} & -\frac{\tilde{J}_k}{2\mathcal{N}} + 1 \end{pmatrix} \begin{pmatrix} a_k \\ a_{-k}^\dagger \end{pmatrix}, \quad (19)$$

where $a_k = \frac{1}{\sqrt{N}} \sum_j e^{ikj} a_j$ and $\tilde{J}_k = \sum_l J_l \cos(kl)$; specifically, we have $\tilde{J}_{k=0} = \mathcal{N}$. The dispersion relation is then given by

$$\omega_k = \sqrt{1 - \tilde{J}_k/\mathcal{N}}. \quad (20)$$

One can see that $k = 0$ is the zero (or, the Goldstone) mode since $\omega_{k=0} = 0$. For $\alpha > 1$, the dispersion ω_k depends continuously on k in the thermodynamic limit ($N \rightarrow \infty$) and vanishes with k as $k \rightarrow 0$. In contrast, for $\alpha < 1$, the spectrum remains discrete and the zero mode at $k = 0$ has a finite energy difference from the next mode at $k = 2\pi/N$ (ref. 36). The gapped modes will not contribute to critical fluctuations and one can furthermore show that the zero mode exhibits subextensive fluctuations, hence the stability of the CSB phase against fluctuations. To analyse the effect of disorder, we note that the disorder in J_{ij} effectively couples the zero mode to the gapped modes of the system. Such coupling is generically irrelevant, and the CSB phase will be stable.

The behaviour of the XY phase under disorder is beyond the scope of this work; however, one generally expects that disorder would lead to a suppression or possible destruction of long-range correlations and could even lead to localization phenomena.

Data availability

Data that support the findings of this study are available from the corresponding authors on reasonable request.

31. Kim, K. et al. Entanglement and tunable spin-spin couplings between trapped ions using multiple transverse modes. *Phys. Rev. Lett.* **103**, 120502 (2009).
32. Katz, O. & Monroe, C. Programmable quantum simulations of bosonic systems with trapped ions. *Phys. Rev. Lett.* **131**, 033604 (2023).
33. Pagano, G. et al. Quantum approximate optimization of the long-range Ising model with a trapped-ion quantum simulator. *Proc. Natl Acad. Sci. USA* **117**, 25396 (2020).
34. Jaschke, D., Wall, M. L. & Carr, L. D. Open source matrix product states: opening ways to simulate entangled many-body quantum systems in one dimension. *Comput. Phys. Commun.* **225**, 59 (2018).
35. Kac, M., Uhlenbeck, G. & Hemmer, P. On the Van der Waals theory of the vapor-liquid equilibrium. I. Discussion of a one-dimensional model. *J. Math. Phys.* **4**, 216 (1963).
36. Defenu, N. Metastability and discrete spectrum of long-range systems. *Proc. Natl Acad. Sci. USA* **118**, e2101785118 (2021).

Acknowledgements This work is supported in part by the ARO through the IARPA LogiQ programme; the NSF STAQ, QLCI, RAISE-TAQS and QIS programmes; the AFOSR MURIs on Dissipation Engineering in Open Quantum Systems and on Quantum Verification Protocols; the ARO MURI on Modular Quantum Circuits; the DoE ASCR Quantum Testbed Pathfinder programme; NSF CAREER; AFOSR YIP; and the W. M. Keck Foundation. Support is also acknowledged from the US Department of Energy, Office of Science, National Quantum Information Science Research Centers, Quantum Systems Accelerator.

Author contributions All authors contributed to the experimental design, construction and discussions, and wrote the manuscript. O.K. and L.F. collected the data, and L.F. analysed the results. C.H., Z.-X.G., M.M. and A.V.G. performed analytical and numerical calculation.

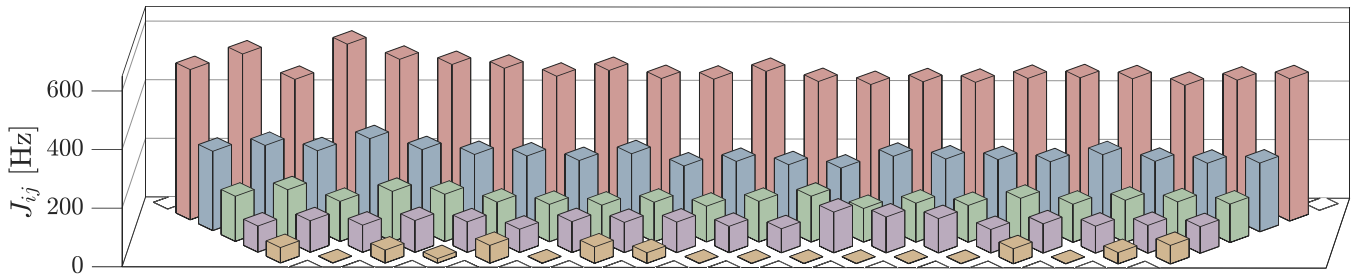
Competing interests C.M. is the chief scientist for IonQ, Inc. and has a personal financial interest in the company. The other authors declare no competing interests.

Additional information

Correspondence and requests for materials should be addressed to Lei Feng, Or Katz or Christopher Monroe.

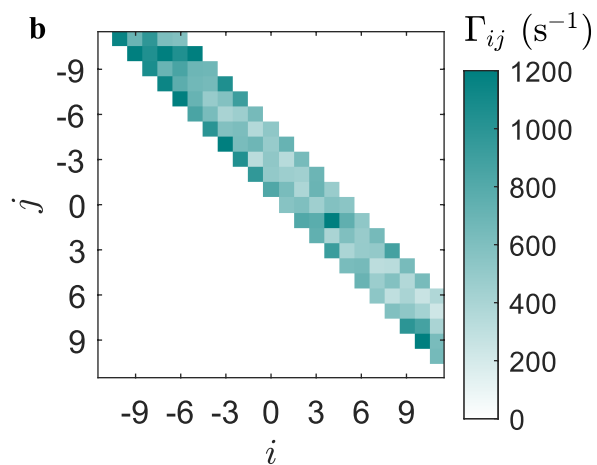
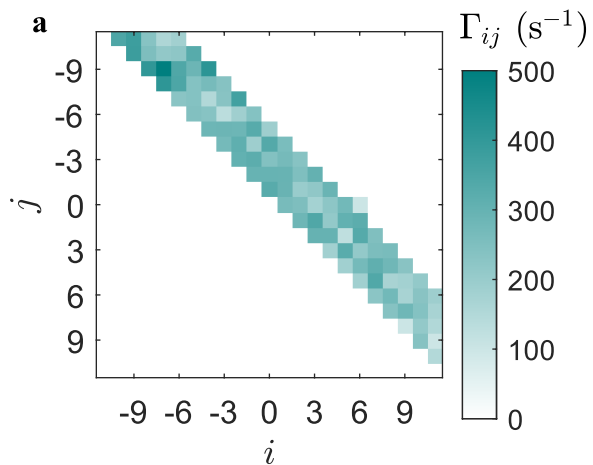
Peer review information Nature thanks the anonymous reviewers for their contribution to the peer review of this work.

Reprints and permissions information is available at <http://www.nature.com/reprints>.



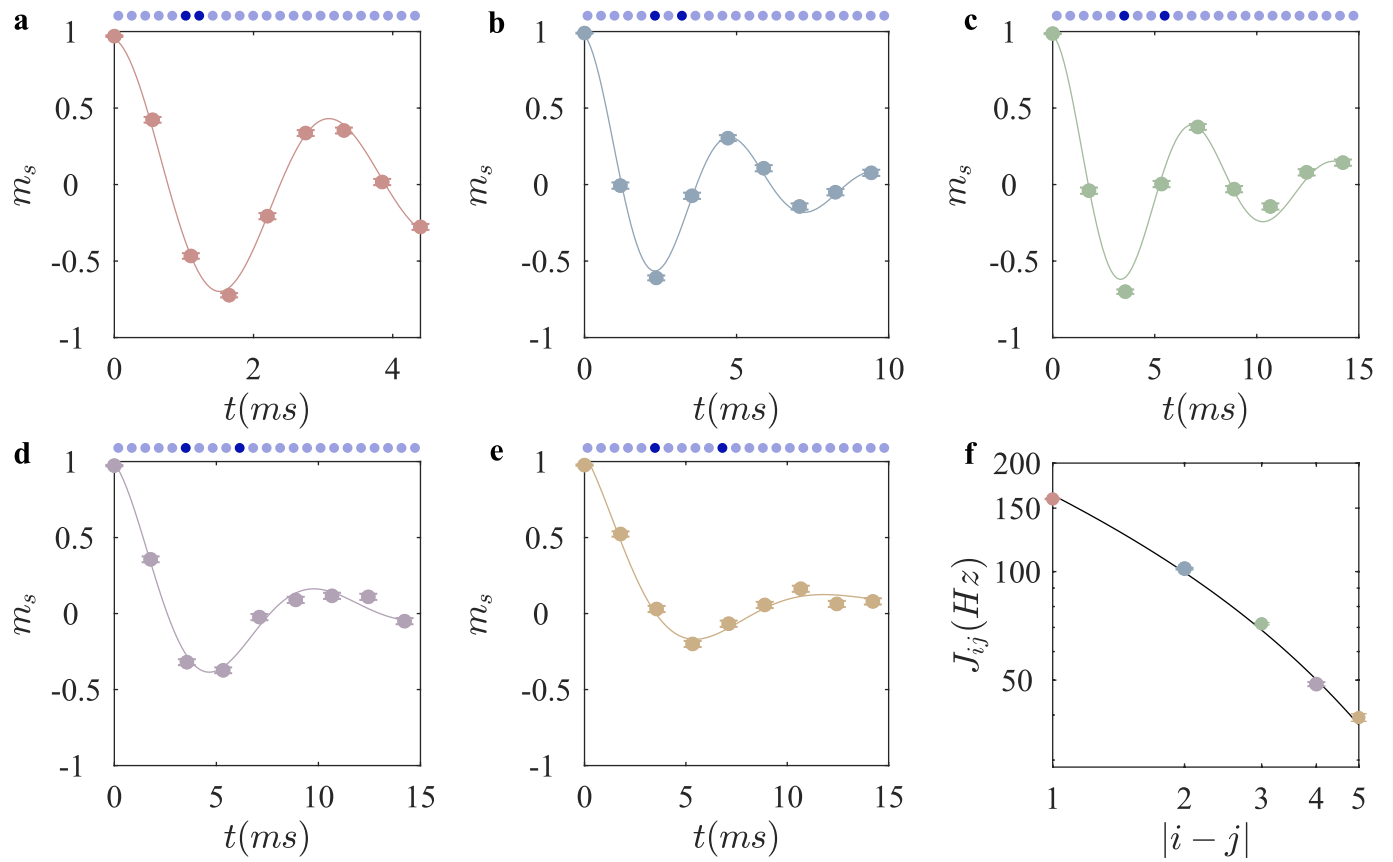
Extended Data Fig. 1 | Partial reconstruction of the interaction matrix in the second experimental configuration. The experimentally reconstructed J_{ij} matrix is shown for a second experimental configuration up to five nearest

neighbors. The full modeled interaction is detailed in the Methods section and is shown in Extended Data Fig. 5. This matrix exhibits long-range interaction, which is nevertheless shorter than the interaction in Fig. 1c.



Extended Data Fig. 2 | Decoherence rate matrix. The measured decoherence rate matrix Γ_{ij} is extracted from the reconstruction protocol for up to five nearest neighbors (see Methods). **a**, The measured relaxation accompanying

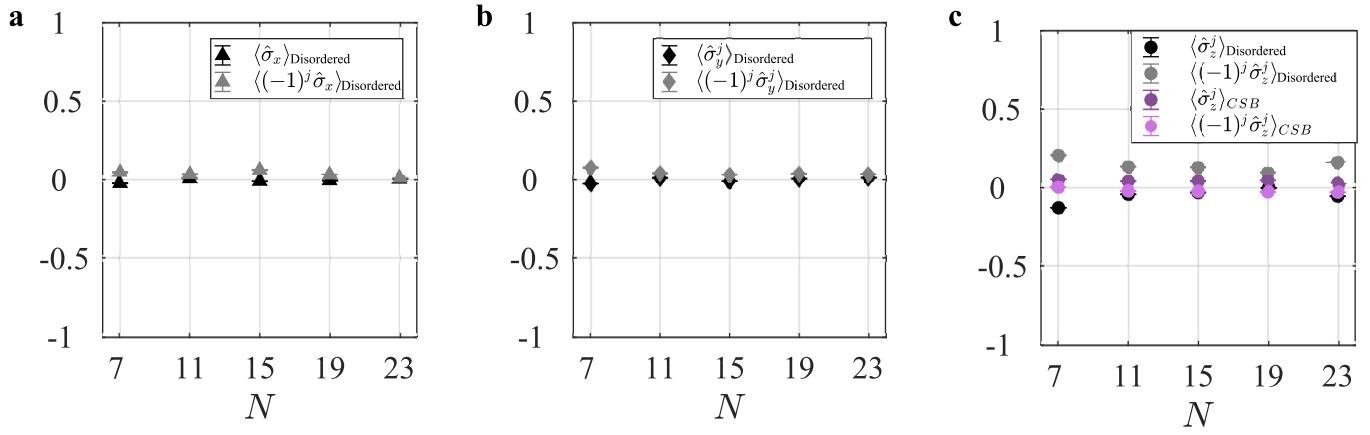
the interaction matrix in the first configuration (Fig. 1c). **b**, The measured relaxation accompanying the interaction matrix in the second configuration (Extended Data Fig. 1).



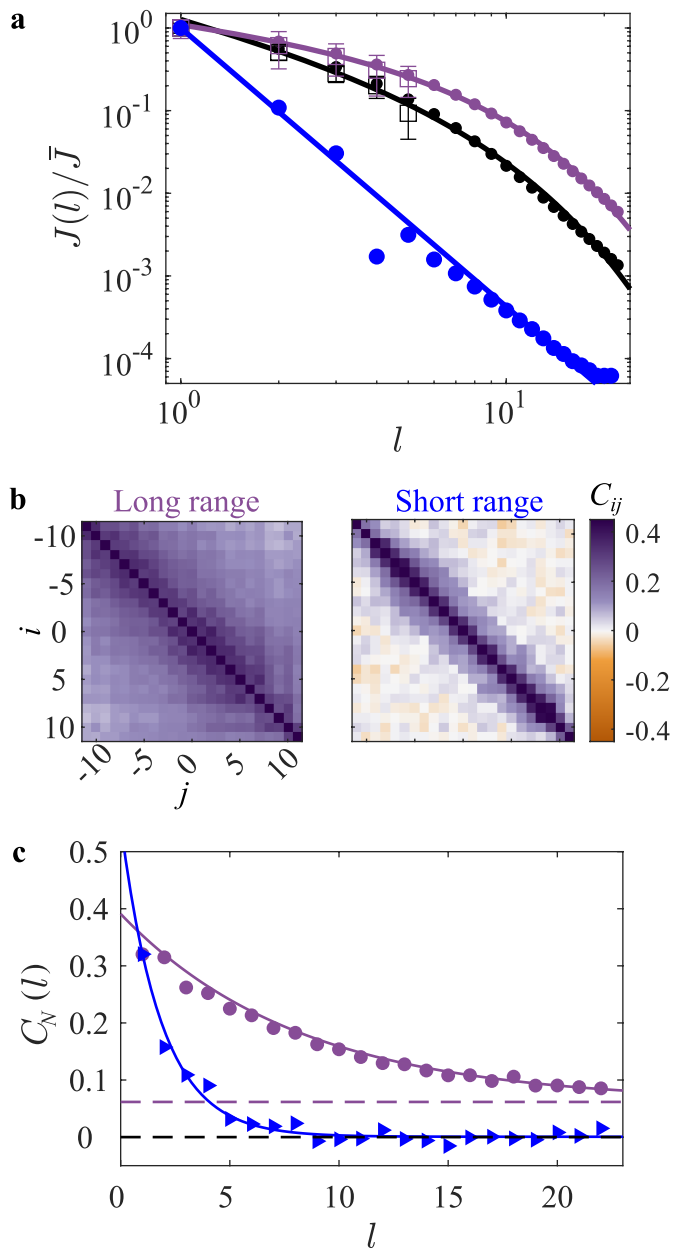
Extended Data Fig. 3 | Demonstration of the reconstruction protocol.

We measure the interactions between the $i = -6$ ion with its up to five-nearest neighbors, by turning on the a single pair of beams addressing two ions a time. Specifically $(i, j) = (-6, 5)$ in **a**, $(-6, 4)$ in **b**, $(-6, 3)$ in **c**, and $(-6, 2)$ in **d** and $(-6, 1)$ in **e**, as indicated by a dark blue sphere. We fit the staggered magnetization $m_s = \frac{1}{2}(\sigma_z^i - \sigma_z^j)$ to the function $y = \cos(\pi g^2 J_{ij} t) e^{-g^2 \Gamma_{ij} t}$ to extract the interaction

strength J_{ij} and the decoherence rate Γ_{ij} . The interaction rate as a function of the inter-ion spacing is shown in **f**. The fitted J_{ij} for $i = -6$ (circles). The black line corresponds to the fit function in Eq. (5) with fitting parameters $\alpha' = 0.44$, $\beta' = 0.19$. The errorbars indicate one standard error of the mean. The exemplary data in this figure corresponds to the interaction matrix in Fig. 1c with a scaling factor $g = 1.3$; see Methods.

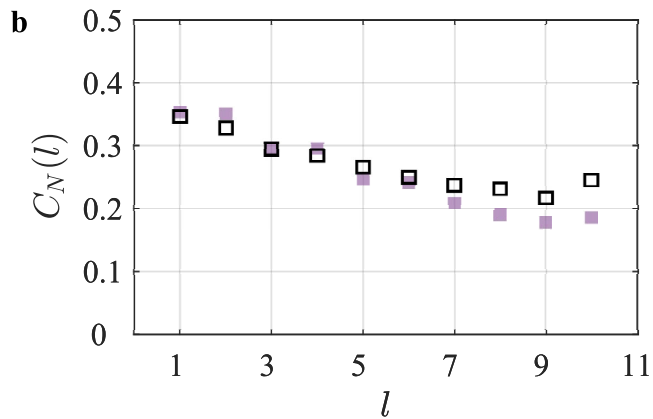
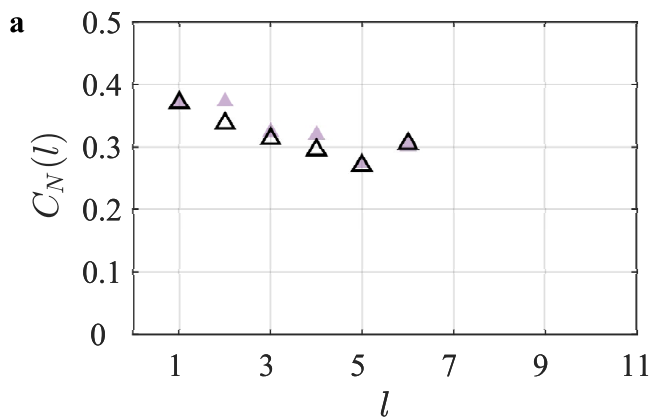


Extended Data Fig. 4 | Average magnetization. The measured regular and staggered magnetization along the x (a), y (b), and z (c) axes for the first configuration (with interaction matrix in Fig. 1c). The errorbars indicate one standard error of the mean.



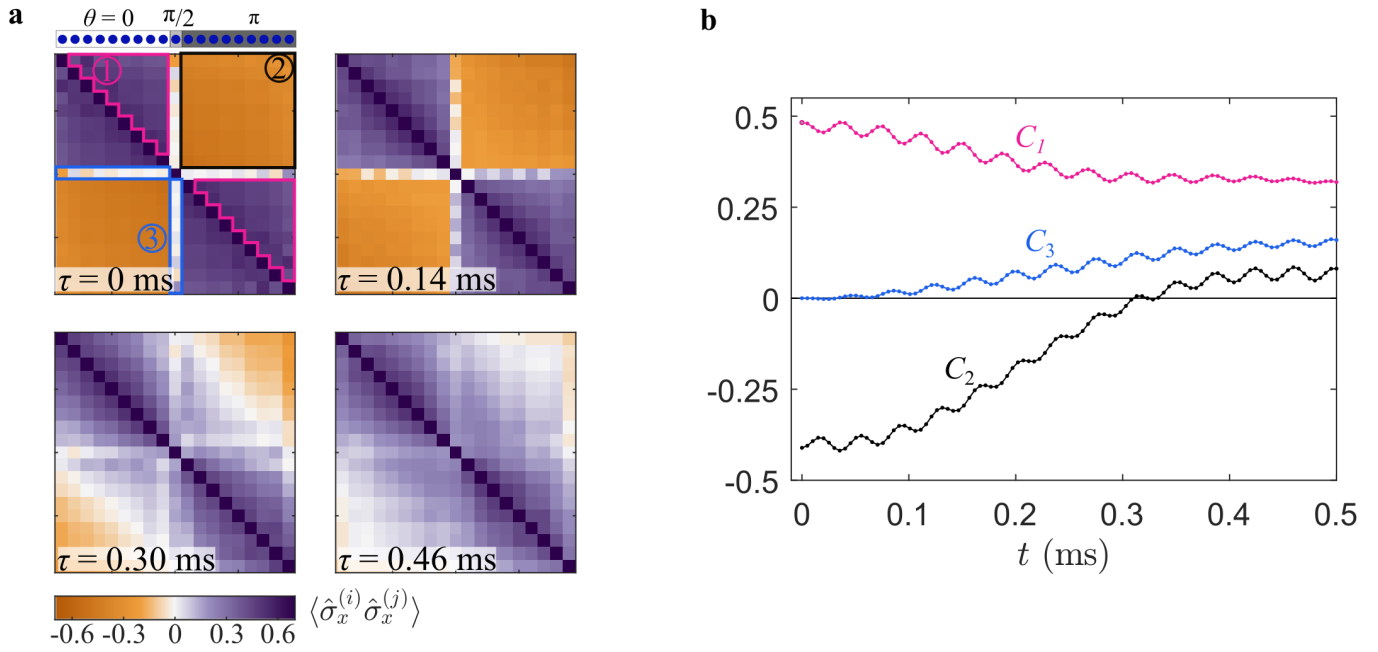
Extended Data Fig. 5 | Modeled interaction and measured correlations.

a, Numerically calculated spin-spin interaction based on Eq. (4) and a simple model of the trapping potential for the three experimental configurations, assuming a harmonic trap for the radial coordinates and a combination of quadratic and quartic potentials for the axial direction. The filled circles indicate the numerically calculated values with no free parameters. The solid lines are fits to the numerical results with a profile of $J(l) = \bar{J} e^{-\beta'(l-1)l^{-\alpha'}}$. The fitted parameters are $\alpha' = 0.44$, $\beta' = 0.19$ for the first configuration (purple), $\alpha' = 1$, $\beta' = 0.19$ for the second configuration (black), and $\alpha' = 3.4$, $\beta' = 0$ for the third configuration (blue). Open squares are the experimental data in two out of the three experimental configurations, where the bars represent the spread of measured values of all pairs at a specific spacing l , namely one standard error of the mean. **b**, Measured spin correlation for the first (left) and the third (right) configuration for the state prepared at the end of the ramp. **c**, Comparison between the spatially averaged correlations $C_N(l)$ for $N = 23$ as a function of inter-spin distance l for the long-range (purple) and the short-range (blue) configurations.



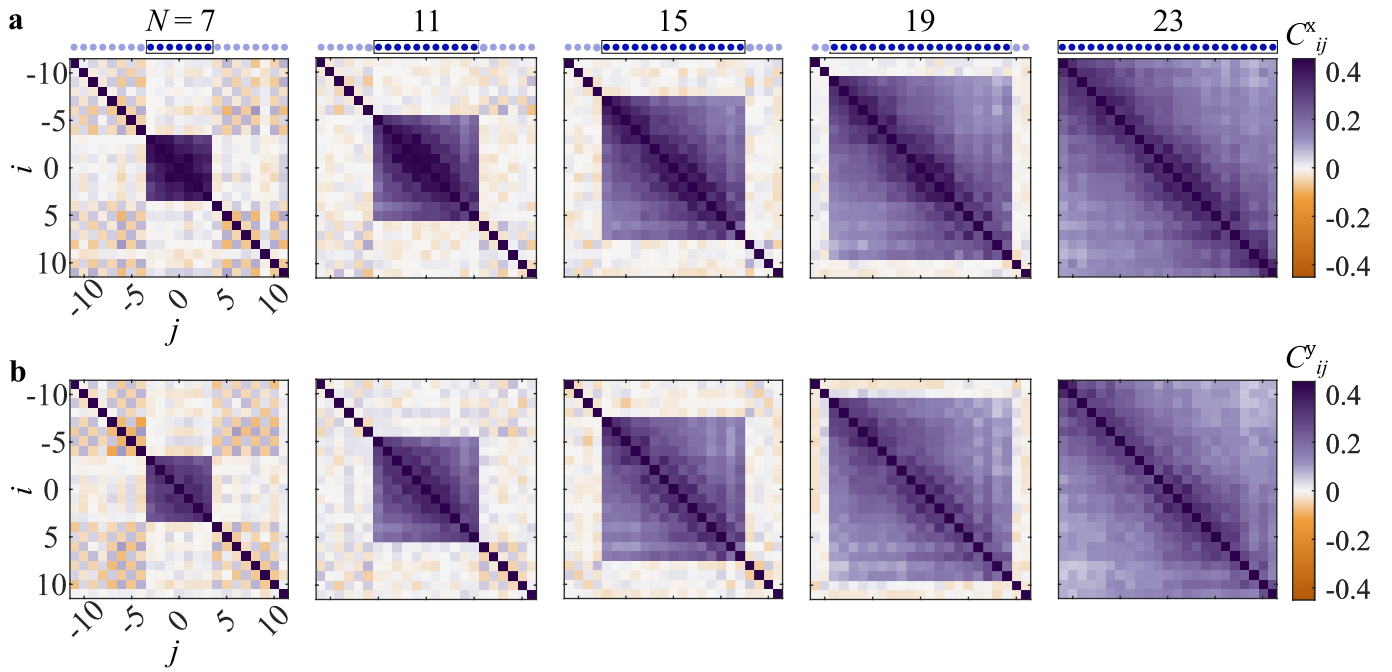
Extended Data Fig. 6 | Numerical simulation of the experiment in the first configuration. **a** and **b** show the comparison of the correlation functions $C_N(l)$ between the experimental data (filled) and numerical results (unfilled) including modeled decoherence. In **a**, the system size is $N=7$, and, in **b**, it is $N=11$.

Article



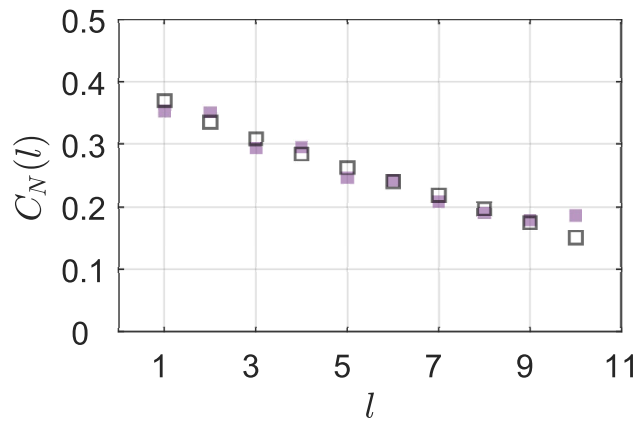
Extended Data Fig. 7 | Numerical simulation of the quench dynamics. We simulate the unitary quench evolution in Fig. 4 (i.e. without considering any decoherence processes). **a**, Measured spin-spin correlations $\langle \hat{\sigma}_x^{(i)} \hat{\sigma}_x^{(j)} \rangle$ developed during the evolution by Eq. (3) for time τ . **b**, Average correlation as a

function of time. The dots in different colors correspond to the correlation averaged within the corresponding colored contours shown in **a** (top left). The fast oscillations are due to the large but finite longitudinal magnetic field B .

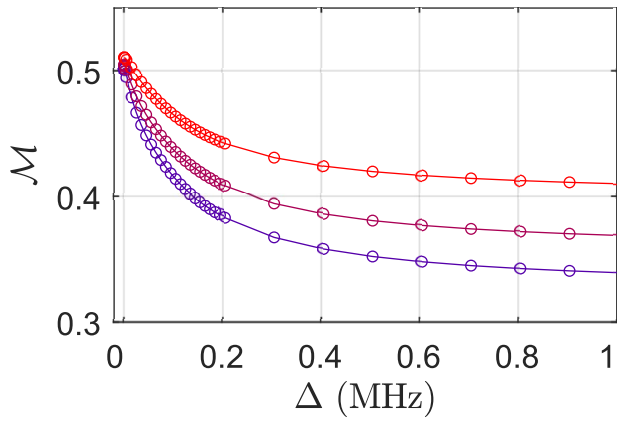


Extended Data Fig. 8 | Long-range correlation. The correlation matrix $C_{ij}^k = \langle \hat{\sigma}_k^{(i)} \hat{\sigma}_k^{(j)} \rangle$, with **(a)** $k=x$ or **(b)** $k=y$, measured in the x and y basis, respectively, for various system sizes of $N=7, 11, 15, 19$, and 23 . This data corresponds to the

first experimental configuration (purple curve in Extended Data Fig. 5a) that leads to the correlations presented in Fig. 3 via the relation $C_{ij} = \frac{1}{2}(C_{ij}^x + C_{ij}^y)$.



Extended Data Fig. 9 | Estimation of effective temperature. Comparison of the correlations $C_N(l)$ between the measured state (Fig. 3b) (purple) and a numerically calculated thermal-state (black) for $N = 11$. The thermal state has an effective temperature $k_B T \approx 0.07 \bar{E}_{\text{int}}$, with $\bar{E}_{\text{int}} = \frac{1}{N} \sum_{i \neq j} J_{i,j}$ denoting the average interaction energy. Here we consider the second experimental configuration presented as a black curve in Extended Data Fig. 5a.



Extended Data Fig. 10 | Simulation of larger spin chains. Numerical simulation of the order parameter $\mathcal{M}(N)$ of the CSB phase in the ground state of $-H$ ($s=1$) for spin chains of different sizes ($N=23$ in red, 49 in magenta, and 89 in blue) as a function of the sideband detuning Δ . The sharp decrease in \mathcal{M} at large Δ (short interaction range) compared to that at small Δ (large interaction range) indicates a phase transition from a disordered phase to the CSB phase.